Optimal airfoil's shapes by high fidelity CFD

Aircraft Engineering and Aerospace Technology
Airc. Eng. Aer. Tech. 0000; **00**:1–17
Published online in Emerald www.emeraldinsight.com. DOI: 10.1108/fld

Optimal airfoil's shapes by high fidelity CFD

ABSTRACT

Purpose - There is an increasing interest in airfoils that modify their shape to adapt at the flow conditions. As an example of application, we search the optimal 4-digit NACA airfoil that maximises the lift-over-drag ratio for a constant lift coefficient of 0.6, from $Re = 10^4$ to 3×10^6.
Design/methodology/approach - We consider a $\gamma - Re_{\theta_t}$ transition model and a $\kappa - \omega$ SST turbulence model with a covariance matrix adaptation evolutionary optimisation algorithm. The shape is adapted by radial basis functions mesh morphing using four parameters (angle of attack, thickness, camber, maximum camber position). The objective of the optimisation is to find the airfoil that enables a maximum lift-over-drag ratio for a target lift coefficient of 0.6.
Findings - The computation of the optimal airfoils confirmed the expected increase with Re of the lift-over-drag ratio. However, while the observation of efficient biological fliers suggests that the thickness increases monotonically with Re, we find that it is constant but for a 1.5% step increase at $Re = 3 \times 10^5$.
Practical implications - We propose and validate an efficient high fidelity method for the shape optimisation of airfoils that can be adopted to define robust and reliable industrial design procedures.
Originality/value - We show that the difference in the numerical error between 2D and 3D simulations is negligible, and that the numerical uncertainty of the 2D simulations is sufficiently small to confidently predict the aerodynamic forces across the investigated range of Re.

KEY WORDS: Transitional models, Reynolds-avaraged Navier-Stokes simulations, large eddy simulations, verification and validation, radial basis functions, covariance matrix adaptation evolution strategy, optimal airfoil thickness

INTRODUCTION

In recent years there has been an increasing interest in morphing airfoils that can operate efficiently across a wide range of Reynolds numbers (Re). For example, a tidal turbine blade operates in a periodic tidal stream and, every three hours, Re varies from 10^4 to 10^6. The blade efficiency would be significantly enhanced if it's sectional airfoil could adapt its shape to the flow conditions (Tully and Viola 2016). The benefit of adopting a variable airfoil geometry has been proven in several applications, including aircraft wings and helicopter rotors (Stanewsky 2001; Barbarino et al. 2011; Kuder et al. 2013), wind and tidal turbine blades (M. Hansen et al. 2006; Barlas and Kuik 2010; Lachenal, Daynes, and Weaver 2013; Tully and Viola 2016). While the research field of airfoil design (O. Smith 1975; Lissaman 1983; Selig 2003) and multi-objective optimisation (Hicks and Henne 1978; Drela 1998; Srinath and Mittal 2010; Minervino, Vitagliano, and Quagliarella 2016) is well established, the optimisation across a wide range of Re is an open area of research. In fact, most of the methods typically used for airfoil optimisation have been originally developed to model specific flow conditions and have been validated only in a limited range of Re. The aim of this paper is to identify and assess a Computational Fluid Dynamics (CFD) method that can be efficiently coupled with an optimisation strategy and that is capable to correctly predict the airfoil performance from $Re = 10^4$ to 3×10^6.

Reynolds number effects

Increasing Re can lead to laminar-to-turbulent transition of the boundary layer and this could postpone or prevent separation. As an example, for a small increase in Re from 2×10^5 to 4×10^5, the lift coefficient C_L of a half cylinder section switches from -0.5 to 0.5 due to the transition in the boundary layer (Bot et al. 2016). At low Re, rough airfoils allow higher maximum lift-to-drag ratio than smooth airfoils due to roughness promoting transition (McMasters and Henderson 1980). As an interesting example, it has been argued that the peaks and valleys of some insect wings, such as the dragonfly *Anisoptera*, could be functional in promoting transition and thus delaying separation (Hu and Tamai 2008).

Transition may occur through three types of mechanisms. For a low levels of free stream turbulence, Tollmien-Schlichting waves or cross-flow instability may grow into turbulence. If laminar separation occurs, the Kelvin-Helmholtz instability in the separated shear layer might lead to turbulence. Finally, high level of free stream turbulence can penetrate into the boundary layer and enable by-pass transition.

If transition occurs in the shear layer at sufficiently high Re (typically higher than 5×10^4 (Carmichael and NASA 1982)), transition might enable reattachment and the formation of a long-type laminar separation bubble (LSB). The long-type LSB has an elongated shape; it covers a significant proportion of the chord length and it is associated with a lower lift and higher drag than the inviscid solution (Crabtree 1959). When the Reynolds number based on the displacement-thickness and the outer velocity at the separation point increase above a critical value (Klanfer and Owen n.d.), or when the pressure recovery across the turbulent mixing region decreases below a critical value (Crabtree 1959), then the long-type LSB burst in a short-type LSB. The latter is thiner and shorter then the long-type LSB, it has minimum effect on the pressure distribution (Crabtree 1959; Ward 1963), and the form factor decreases as much as when transition occurs in the attached boundary layers (McMasters and Henderson 1980). The flow separation and the occurrence of the two different types of LSB make the aerodynamic forces trends highly non linear and difficult to predict.

Available numerical methods

Modelling the laminar-to-turbulent transition is one of the key challenges of CFD and, as shown in the previous section, it is of paramount importance to correctly predict the aerodynamic forces at transitional Re. Between the different methods that have been used for modelling transition, from the less computationally expensive to those that resolve more physics, there are: linear stability theory; low-Reynolds-number turbulent models; the Local-Correlation-based Transition Models (LCTM); Large Eddy Simulations (LES); Detached Eddy Simulations (DES) and Direct Numerical Simulations (DNS). A critical comparison between these methods is available, for instance, in Di Pasquale *et al.* (Pasquale, Rona, and Garrett 2009). The methods based on linear stability theory, such as the e^N method (Smith 1956; Mack 1977; Ingen 2008), are incompatible with large free stream turbulence levels and cannot predict bypass transition. Low-Reynolds-number turbulent models are based on the wall-induced damping of turbulent viscosity and are unable to predict the growth of natural instabilities along streamlines. On the other hand, LES (Sagaut and Deck 2009), DES (Squires 2004; Spalart 2009), and even more DNS (Moin and Mahesh 1998; Wu and Moin 2009), can resolve transition mechanisms but their computational costs (Celik 2003; Sagaut and Deck 2009) are currently incompatible with optimisation algorithms that require the evaluation of a large number of candidates.

The LCTMs could, in principle, predict correctly all the transition mechanisms (F.R. Menter, Langtry, and Völker 2006). In particular, in this paper we test the $\gamma - Re_{\theta_t}$ transition model (Langtry and F. Menter 2005), which is an LCTM that can be used with the $\kappa - \omega$ SST turbulence model for Reynolds-Averaged Navier-Stokes (RANS) simulations. This transition model is based on two transport equations: one for the intermittency, which allows the growth of the natural instabilities along streamlines; and one for the transition momentum thickness, which allows the effect of free stream turbulence to penetrate into the boundary layer.

DOI: 10.1002/fld

Objectives and structure of the paper

In this work, we assess the potentialities offered by the $\gamma - Re_{\theta_t}$ transition model for airfoil optimisation across a range of Re that spans from 10^4 to 3×10^6. The airfoil geometry and the angle of attack are optimised using an evolutionary optimisation strategy coupled with radial basis functions mesh morphing for the mesh adaption onto the new shape. The geometry is constrained to a 4-digit NACA airfoil, which is defined by the thickness t, the camber f, and the chordwise coordinate of the maximum camber position x_f. The objective of the optimisation is to find the airfoil that enables a maximum lift-over-drag ratio for a target lift coefficient of 0.6, which is arbitrarily chosen as a typical value for cruising flight.

We consider bi-dimensional unsteady RANS (2D URANS) simulations and we perform verification and validation (V&V) of the force coefficients. The *verification* enables the quantification of the uncertainty due to the *numerical* error, i.e. the error between the numerical solution and the exact solution of the system of equations solved. The *validation* allows the determination of the *modelling* error, which represents the degree to which these equations, boundary and initial conditions are an accurate representation of the real physics. The numerical uncertainty is assessed for both a reference test case of an SD7003 airfoil, for which experimental data is available, and for the optimal 4-digit NACA airfoils. We further investigate the numerical error comparing 2D URANS simulations with 3D URANS, LES and Xfoil.

The rest of the paper is structured as follow. In section (Method), we present the 2D URANS solver setup (sec.), how it is coupled with the optimisation algorithm (sec.), how we assess the numerical uncertainty (sec.) and the modelling error (sec.). In section (Results), firstly we present the numerical uncertainty for the reference test case and for the 4-digit NACA airfoils (sec.), and the analysis of the the modelling error for the reference test case (sec.). Successively we discuss the optimal shapes of the 4-digit NACA airfoils (sec.), the trends with Re of the lift-to-drag ratio (sec.) and the optimal thickness (sec.). The main outcomes of this work are summarised in the Conclusions (sec.).

METHOD

In this section we present the method of the study. Firstly we provide an overview of the 2D URANS simulations and of the optimisation problem, and successively we discuss how we estimate the numerical and the modelling errors.

2D URANS solver setup

We solve the 2D URANS equations for Newtonian fluids and incompressible flow for an airfoil in open air using a segregated finite-volume solver (Ansys Fluent version 17.2). We use the $\gamma - Re_{\theta_t}$ transition model and the $\kappa - \omega$ SST turbulence model. The numerical schemes are second-order accurate both in space and time, and implicit in time. The domain is $20\,c \times 20\,c$, where c is the length of the airfoil's chord. A parametric C-type structured mesh is built near the airfoil, surrounded by an unstructured triangular mesh (figure 3a). The mesh is adapted onto the new shape using a radial basis function mesh morphing software (RBF Morph Ansys Fluent Add On) for every tested geometry according to the approach presented in (Biancolini, Viola, and Riotte 2014; Biancolini, Costa, et al. 2016; Biancolini 2018) . For each Re, the grid is uniformly scaled in order to achieve a non-dimensional wall-coordinate $y^+ \leq 0.5$. We use a no-slip condition on the airfoil surface. We prescribe uniform velocity on the upstream and bottom boundaries, where the turbulence intensity is $I = 1\%$ and the turbulent length scale is $L_t = 0.005\,c$, and a constant pressure on the downstream and upper boundaries.

Prepared using Overleaf
DOI: 10.1002/fld

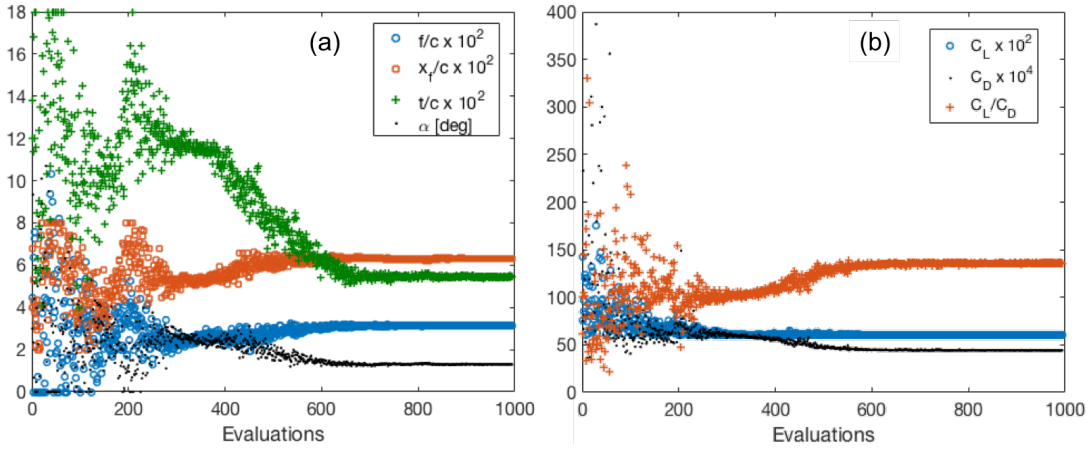

Figure 1. Example of convergence history for $Re = 10^6$ of (a) the design variables and (b) the force coefficients.

Optimisation algorithm

We solve the following optimisation problem:

$$\begin{aligned} \min \mathrm{J}(\boldsymbol{X}) \quad &= C_D + \left(1 - \tfrac{C_L}{0.6}\right)^2 \\ \text{s.t.} \quad &\boldsymbol{X} \succ \boldsymbol{X_{LB}} \\ &\boldsymbol{X} \prec \boldsymbol{X_{UB}} \end{aligned} \tag{1}$$

where $\boldsymbol{X} = (f/c, x_f/c, t/c, \alpha)$, $\boldsymbol{X_{LB}} = (0, 0.2, 0.04, 0)$, $\boldsymbol{X_{UB}} = (0.12, 0.8, 0.18, 12)$ and α are degrees. The coefficients C_D and C_L are the time-averaged drag and lift forces, respectively, divided by the dynamic pressure and the chord. The forces are computed over a period spanning from $80\, c/U_\infty$ to $160\, c/U_\infty$, where U_∞ is the free stream flow speed. The symbol $\succ$ ($\prec$, respectively) indicates that each element of the left hand side vector is greater (smaller, respectively) than each element of the right hand side vector. The aim of the second term on the right hand side of equation 1 is to penalise the deviations of C_L from its target value of 0.6. In other words, a set of optimal design values $\boldsymbol{X'}$ is looked for, such that a compromise is found between minimising C_D and deviating from $C_L = 0.6$. Different penalty terms would lead to different optima, however the magnitude of these differences are such that they can be assumed negligible in the present context.

The initial guessed values is $\boldsymbol{X_0} = (0.04, 0.4, 0.12, 2)$. The use of bounds on $\boldsymbol{X}$ limits the search to a range of realistic values. The optimal solution lies in the interior of the bounded domain and not on the bounds. The objective function is evaluated with the flow solver, which is coupled with a stochastic gradient-free optimisation algorithm (Chapin, De Carlan, and Heppel 2011). A Covariance Matrix Adaptation Evolution Strategy (CMA-ES) is used for its robustness and effectiveness in handling noisy, non-linear, multimodal objective functions (N. Hansen et al. 2011). Gradient-free algorithms are well suited when dealing with noisy functions, or when the evaluation of the cost function and of the constraints (when applicable) is computationally expensive.

Figure 1 shows an example of convergence history of the design variables and force coefficients at $Re = 10^6$. Computations run in parallel on 8 cores on a Linux workstation based on Intel Xeon E5 of 2.4 GHz with 32 GB of RAM. For every Re, the optimisation converges to an optimum airfoil with less than 1000 evaluations and with a wall clock time of the order of one hour per evaluation.

Uncertainty quantification

We perform the V&V of the C_L and C_D computed with 2D URANS simulations. We consider the test case of an SD7003 airfoil at $\alpha = 4°$ and $Re = 6 \times 10^4$, for which experimental data is available in the literature. These conditions are particularly challenging for CFD simulations because of the presence of a long LSB, whose size and position are affected by the background turbulence.

DOI: 10.1002/fld

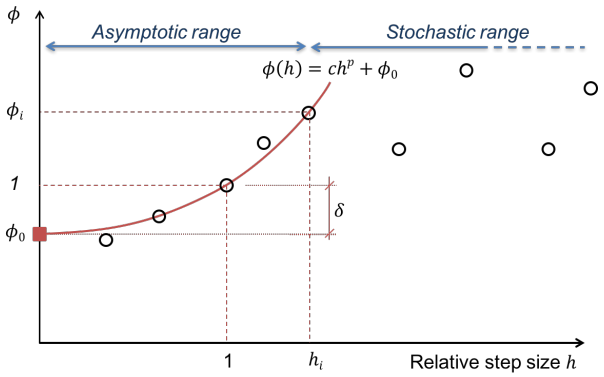

Figure 2. Schematic diagram of the method to compute the grid and time step uncertainties.

The measured forces were corrected for the blockage effect of the finite cross sectional area of the wind tunnel facility and, hence, we use the same large computational domain size as the 2D URANS simulations used for the optimisation of the airfoil. The same boundary conditions as for the optimisation are used, but for the onset turbulent intensity and turbulent length scale that are set as for the experiments of Selig *et al.* (Selig 1995) to $I = 0.10\%$ and $L_t = 0.0025\,c$.

The numerical uncertainty is quantified using the method proposed by Viola *et al.* (Viola, Bot, and Riotte 2013), which is based on the trends of C_L and C_D for different values of the time step, grid size, precision of the machine, and number of iterations. This method was initially developed for yacht sail aerodynamics, but it can be applied to any other application. The method is as follows.

The 95% confidence interval of any computed value ϕ_{cfd} (in this paper ϕ_{cfd} is either C_L or C_D) is given by $\phi_{\text{cfd}} \pm U_{\text{num}}\phi_{\text{cfd}}$, where the numerical uncertainty U_{num} is the combination of the uncertainties due to the grid (U_g), the time step (U_t), the round off error (U_r), and the convergence (U_c):

$$U_{\text{num}} = \sqrt{U_g^2 + U_t^2 + U_r^2} + U_c, \tag{2}$$

Uncertainty due to the grid. The method to compute U_g and U_t is conceptually identical. To compute U_g, a number of simulations $n_g > 3$ with different grid resolutions are performed. The reference grid, for which the uncertainty is computed, can be either uniformly refined or uniformly coarsened. We define the relative step size h_i as the ratio between the cell sizes of the $i-$th grid and the reference grid; and ϕ_i as the ratio between the force coefficients computed with the $i-$th grid and the reference grid (figure 2). When $h \to 0$, the fit of ϕ_i should converge to an horizontal asymptote $\phi = \phi_0$ with the order p of the adopted numerical scheme. Given that different schemes are used to solve the coupled system of equations, p is generally unknown. Therefore, a curve

$$\phi(h) = ch^p + \phi_0 \tag{3}$$

is fitted through the set of ϕ_i. More than three grids should be computed and therefore the parameters c, p and ϕ_0 can be estimated by least square method. We also compute the standard error of the fit,

$$\sigma_{\text{fit}} = \sqrt{\frac{\sum_1^{n_g} (\phi_i - \phi(h_i))}{N}}, \tag{4}$$

where $\phi(h_i)$ is the value of the function ϕ evaluated in h_i, and $N = n_g - 3$ is the number of degrees of freedom of the fit.

The extrapolated value ϕ_0 is the expected value of ϕ for an infinitely fine grid. This allows estimating the error of the reference grid (cf. figure 2) as

$$\delta = |1 - \phi_0|. \tag{5}$$

DOI: 10.1002/fld

Table I. Tested grids of the SD7003 airfoil at $Re = 6 \times 10^4, \alpha = 4^\circ, I = 0.10\%$.

	Grid 1	Grid 2	Grid 3	Grid 4 (ref)	Grid 5	Grid 6
Number of cells	3.3×10^3	6.4×10^3	4.3×10^4	5.4×10^4	1.3×10^5	4.7×10^5
Maximum y^+	2	1	0.5	0.1	0.1	0.05

The grid uncertainty is then given by

$$U_g = 1.25\,\delta + \sigma_{\text{fit}}, \tag{6}$$

where 1.25 is a safety factor taken from the work of Roache (Roache 1998).

The main limitations of the proposed method is that we apply the least square method when the standard deviation of the error is not constant, but it increases with h. This could be overcome, for instance, doing the logarithmic of equation 3 and then using a linear fit instead of a non linear fit. However, given than ϕ_0 is unknown, it's value should be optimised minimising the residuals of the fit, making the V&V unnecessarily over-complicated.

Table I shows the number of cells and the maximum y^+ of the first cell centre for each grid, while figure 3a shows the reference grid (Grid 4) in the near-wall region. This grid has the same chordwise and wall-normal resolution as the 2D URANS simulations of the optimal airfoils.

Other sources of uncertainty. A virtually identical procedure is used to compute U_t, where six different time steps substitute the different grids used for the computation of U_g. The reference time step is $\Delta t = 0.05 c/U_\infty$, where U_∞ is the free stream velocity, and a range of Δt from $0.0025\,c/U_\infty$ to $2.48\,c/U_\infty$ is explored.

The uncertainty due to the convergence U_c is the 95% confidence interval in the estimate of the mean force coefficient in the time interval from $80\,c/U_\infty$ to $160\,c/U_\infty$:

$$U_c = 1.646 \frac{\sigma}{\sqrt{N_{\text{it}}}}. \tag{7}$$

where σ is the standard deviation of the $N_{\text{it}} = 1600$ observations within this time interval.

The round off error is estimated by running the simulations in both single and double precision. Denoted with ϕ_r the ratio between the force coefficients computed in single and double precision, we estimate the error as

$$\delta_r = |1 - \phi_r|, \tag{8}$$

and we compute the uncertainty as

$$U_r = 3\,\delta_r, \tag{9}$$

where 3 is a safety factor.

As discussed in the Results (section), the grid uncertainty of the SD7003 airfoil is one order of magnitude larger than the other uncertainties. Therefore, for the optimum 4-digit NACA airfoils at $Re = 10^4$, 10^5 and 10^6, we consider only the grid uncertainty. For each Re, the grid is uniformly refined twice by halving every cell.

Modelling error

Validation. The validation against experimental data allows an estimate of the modelling error of ϕ_{cfd}. This is given by the difference between the total error E and and the validation uncertainty U_{val}, which are defined as

$$E = \phi_{\text{cfd}} - \phi_{\text{exp}}, \tag{10}$$

and

$$U_{\text{val}} = \sqrt{U_{\text{num}}^2 + U_{\text{exp}}^2}, \tag{11}$$

where ϕ_{exp} is the experimental estimate and U_{exp} is the experimental uncertainty. If $|E| > U_{\text{val}}$ then the numerical error has the sign of E. Conversely, if $|E| \leq U_{\text{val}}$ then ϕ_{cfd} is validated at the level of U_{val} and the modelling error is relatively too small to be assessed.

DOI: 10.1002/fld

Comparison with other models. In order to gain more insight into the modelling error, we compare the aerodynamic forces, the surface pressures and the velocity field computed with different models: Xfoil, 2D URANS, 3D URANS and LES. Unfortunately, the experimental results of Selig *et al.* (Selig 1995) do not include information on the flow field, therefore we compare with the measurements of Ol *et al.*. (Ol et al. 2005), which instead do not include force measurements. We also consider a slightly higher turbulence intensity, $I = 0.28\%$, in order to compare our results with those of Zhang *et al.* (Zhang, Hain, and Kähler 2008).

Xfoil is an inviscid linear-vorticity panel code coupled with a two-equation lagged dissipation integral method (Drela 1989). Transition is computed with the e^N method. Following the experimental correlations proposed by Mack (Mack 1977; Ingen 2008), we set the N_{crit} value to 5.7 corresponding to the free stream turbulence intensity of the wind tunnel (Zhang, Hain, and Kähler 2008). The grid resolution and solver setting are kept as consistent as possible between the different Navier-Stokes models, so that the differences between 2D URANS and 3D URANS can largely be attributed to the additional dimension, and the differences between 3D URANS and LES can be attributed to the turbulence model.

The domain size and the turbulent intensity used for this comparison are different from those used for the V&V because of the different experimental conditions. The experiments of Selig *et al.* (Selig 1995) included an accurate measure of the aerodynamic forces and, therefore, are used for the V&V, while Zhang *et al.* (Zhang, Hain, and Kähler 2008) performed flow measurements with particle image velocimetry (PIV) and thus we use these tests for the analysis of the modelling error. PIV measurements cannot be corrected for the blockage effect, and hence the computational domain matches the test section of this latter experiment, that is $6.25\,c$ long, $1.65\,c$ wide and $1.25\,c$ high. Since this study of the modelling error focuses on the flow field near the foil and not on the aerodynamic forces, which were not measured during the experiment, we used a relatively short domain in the spanwise direction. This could lead to overestimating the drag. Hence, future work might include a sensitivity study of the effect of the streamwise computational domain size.

We set a no-slip condition on the airfoil surface, a Dirichlet-type velocity condition on the upstream boundary, a symmetry condition on the top and bottom boundaries, and a Neumann-type pressure condition on the outlet boundary. For the 3D URANS and LES simulations, we set a symmetry condition on the side boundaries. If we used a no-slip condition for the side walls of the computational domain, we would have to resolve the boundary layer on the walls of the facility. Conversely, the use of the symmetry condition allows focusing the grid resolution in the region near the airfoil.

In order to achieve a grid that is consistent between the three models - 2D URANS, 3D URANS and LES - we build a new multi-block structured grid (figure 3b), where the resolution near the airfoil is the same as the reference grid (figure 3a). This new grid used for the 2D URANS model is extruded spanwise by 1/3$^{\mathrm{rd}}$ of the airfoil chord to make a 3D grid that is equally suitable for the 3D URANS and LES models. In general, grid requirements for URANS and LES are very different. In particular, the grid spacing in both the streamwise and spanwise directions must be lower for LES than URANS. In the present case, however, a high streamwise grid resolution is used across the whole foil for the 2D URANS simulations in order to accurately resolve separation and reattachment, which occurs at different positions along the chord at every Re. Further, the grid used for the 3D URANS simulations is made with high spanwise resolution making it also suitable for the LES simulation. The 2D grid has 6.4×10^3 cells while the 3D grid has 6×10^6 cells. The thickness of the near-wall cells in the wall-normal direction is $\Delta y = 4 \times 10^{-4}\,c$, which allows $y^+ < 1$. The streamwise cell aspect ratio is $\Delta x/\Delta y = 2$ and the spanwise cell aspect ratio is $\Delta z/\Delta y = 7$. A grid study was not performed for the 3D RANS and LES, and it should be considered for future work.

For the LES, we use a dynamic Smagorinsky-Lilly model for the sub-grid stresses, a bounded central differencing scheme for the spatial derivatives, a second order implicit scheme for the unsteady term in the momentum equation, and a SIMPLE algorithm for time marching with $\Delta t = 0.0025\,c/U_\infty$. A spectral synthesiser method (Smirnov, Shi, and Celik 2001) is used to achieve onset turbulence with $I = 0.285\%$ and $L_t = 0.0075\,c$. The turbulence intensity decays from the inlet to the airfoil location, where $I = 0.280\%$ as reported in the experiments.

DOI: 10.1002/fld

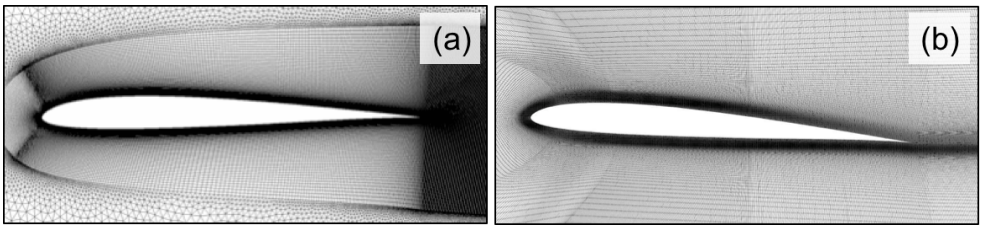

Figure 3. Reference grids around the SD7003 airfoil used for the estimation of (a) the numerical uncertainty of the 2D URANS simulations and (b) the modelling error by comparison of the 2D URANS, 3D URANS and LES models.

Table II. V&V on the SD7003 airfoil at $Re = 6 \times 10^4, \alpha = 4^\circ, I = 0.10\%$.

	C_L	C_D
Experiments (Selig 1995)	0.570	0.017
2D URANS	0.584	0.0208
U_g	0.8%	0.1%
U_t	$< 10^{-5}$	$< 10^{-5}$
U_r	$< 10^{-5}$	$< 10^{-5}$
U_c	$< 10^{-5}$	$< 10^{-5}$
U_{num}	0.8%	0.1%
$\lvert E \rvert$	2.5%	22%
U_{exp}	1.5%	NA
U_{val}	1.7%	NA
Validated at a level of U_{val}?	No	NA

RESULTS

The results are organised as follows. Firstly we discuss the our estimate of the numerical and modelling errors. Successively we present the results of the optimisation for different Re. Finally, we discuss the trends of the maximum efficiency and optimum thickness across with Re.

Uncertainty quantification

Table II summarises the results of the V&V of the 2D URANS computations. The numerical uncertainty of C_L is $U_{\text{num}} = 0.8\%$, while the experimental uncertainty is $U_{\text{exp}} = 1.5\%$ (Selig 1995), which results in a validation uncertainty of $U_{\text{val}} = 1.7\%$. The absolute value of the error on the C_L, $|E| = 2.5\%$, is higher than U_{val} and thus C_L is not validated at the level of 1.7%. The simulation over estimate C_L but the error is not much higher than the validation uncertainty, leading to a low confidence in the sign of the modelling error. This error is further investigated in the next section (section).

The numerical uncertainty of C_D is 0.1%. Unfortunately Selig *et al.* (Selig 1995) did not provide a value for the experimental uncertainty and thus C_D could not be validated. The absolute error of C_D is similar to the one of C_L, which is about 0.5% of the dynamic pressure. However, given the smaller absolute value of C_D compared to C_L, the relative error of C_D is significant. For the present application, an error of 22% is sufficiently small compared to the differences in C_D of ca. 300% for every tenfold increase in Re (cf. table III).

For both C_L and C_D, the grid uncertainty is one order of magnitude higher than the other uncertainties and thus $U_{\text{num}} \approx U_g$. We assume that the other sources of numerical uncertainties are negligible also for the 4-digit NACA airfoils. Therefore, we compute only U_g for the optimal airfoils. We consider $Re = 10^4$, 10^5 and 10^6. Table III shows the number of cells, the maximum y^+ and grid uncertainties for the reference grid at each Re. As for the SD7003 airfoil at $Re = 6 \times 10^4$,

DOI: 10.1002/fld

Table III. Reference grids and U_g for the optimum 4-digit NACA airfoils.

Re	10^4	10^5	10^6
Number of cells	23 000	34 000	64 000
Max (y^+)	0.4	0.07	0.01
C_L	0.57	0.64	0.60
C_D	0.0397	0.0141	0.00425
U_g of C_L	8.4%	3.1%	0.003%
U_g of C_D	19.3%	6.2%	2.1%

Table IV. Comparison with other authors for the SD7003 airfoil at $Re = 6 \times 10^4, \alpha = 4^\circ, I = 0.10\%$.

Model	Reference	I	C_L	C_D	x_s/c	x_t/c	x_r/c
Exp	Selig *et al.* (Selig 1995)	0.10	0.570	0.017	NA	NA	NA
Exp	Ol *et al.*. (Ol et al. 2005)	0.10	NA	NA	0.30	0.53	0.62
Xfoil	Present results	0.10	0.618	0.019	0.22	0.54	0.57
2D URANS	Radespiel *et al.* (Radespiel, Windte, and Scholz 2007)	0.08	0.60	0.020	NA	0.57	0.62
2D URANS	Present results	0.10	0.584	0.0208	0.20	0.50	0.70
LES	Catalano and Tognaccini (Catalano 2010)	0.10	0.63	0.0225	0.21	0.53	0.65

the grid uncertainties are higher for C_D than for C_L. U_g decreases with Re both for C_L and C_D. The uncertainties computed for the SD7003 airfoil at $Re = 6 \times 10^4$ are similar to those computed for the optimum 4-digit NACA foil at $Re = 10^5$. The maximum uncertainty is U_g of C_D (19.3%) for the lowest tested Re (10^4). Recalling that C_D decreases by about 300% for a tenfold increase in Re, the maximum value of U_g of C_D is sufficiently small to compute the trend of C_D across the proposed range of Re.

Modelling error

In order to investigate the source of the modelling error, we compare the flow fields computed with our simulations and the experimental and numerical results of other authors. Table IV shows C_L, C_D, and the chordwise coordinates of the separation point (x_s), of the transition point (x_t) and of the reattachment point (x_r). The transition point is defined as the locum where $\langle u'v' \rangle / U_\infty^2 = 10^{-3}$, where u' and v' are the velocity fluctuations in the drag and lift directions, respectively.

Between this set of results, all numerical simulations over-predict C_L and C_D by a similar amount. The minimum C_L is computed by our 2D URANS simulations, while only Xfoil predicts a slightly lower C_D than 2D URANS. All numerical simulations predicts an earlier separation point than the experiments, and a similar transition and reattachment point. This analysis suggests that the modelling error is not due to the 3D effect or to the turbulence model.

We further investigate the modelling error considering a different set of experiments (Zhang, Hain, and Kähler 2008), where the turbulence intensity is $I = 0.28\%$ instead of $I = 0.10\%$. We model these experiments with Xfoil, 2D URANS, 3D URANS and LES. Table V shows a summary of the results. All models over-predict C_L by more than the 2D URANS simulations, and only Xfoil predicts a closer C_D to the experimental value. With the higher turbulence intensity, x_s/c is well predicted by all models. Both URANS simulations made a similar prediction.

For both values of turbulence intensity, the transition point x_t/c is better predicted by LES. The region of turbulent flow near the airfoil is shown by the contour of $\langle u'v' \rangle / U_\infty^2$ in figure 4, which also includes the experimental results (Zhang, Hain, and Kähler 2008). LES also predicts a higher growth rate of turbulent fluctuations than the other models, resulting in an earlier reattachment and a thinner turbulent boundary layer (cf. also figure 5).

Figure 5 shows the shape of the LSB and the growth of the reattached boundary layer through streamlines and contours of non-dimensional flow speed $|\boldsymbol{u}|/U_\infty$, where $|\boldsymbol{u}|$ is the magnitude of the velocity vector. The shorter LSB and the thinner reattached boundary layer of the LES solution result

Prepared using Overleaf
DOI: 10.1002/fld

Table V. Summary of results for the SD7003 airfoil at $Re = 6 \times 10^4, \alpha = 4^\circ, I = 0.28\%$.

Model	Reference	I	C_L	C_D	x_s/c	x_t/c	x_r/c
Exp	Zhang *et al.* (Zhang, Hain, and Kähler 2008)	0.28	NA	NA	0.21	0.40	0.51
Xfoil	Present results	0.28	0.605	0.018	0.24	0.48	0.52
2D URANS	Present results	0.28	0.586	0.0222	0.18	0.46	0.64
3D URANS	Present results	0.28	0.669	0.0237	0.21	0.45	0.63
LES	Present results	0.28	0.670	0.0219	0.22	0.42	0.57

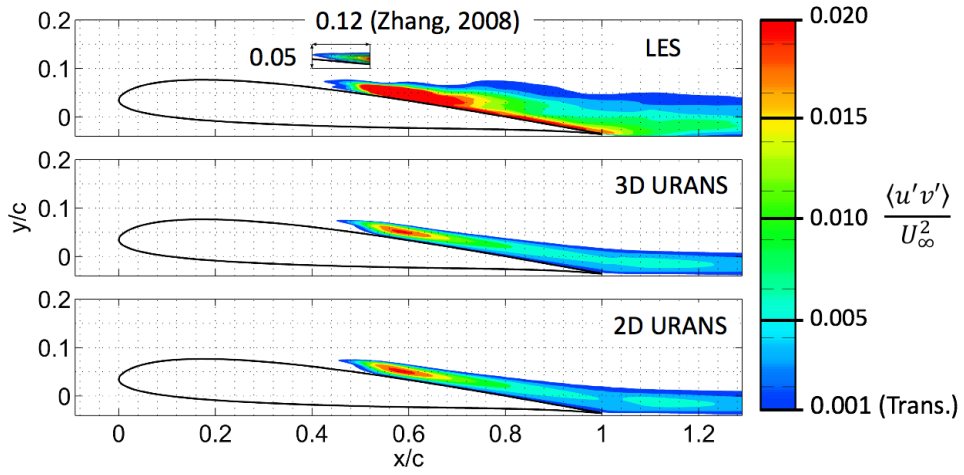

Figure 4. Contours of Reynolds stresses around the SD7003 airfoil tested at $Re = 6 \times 10^4, \alpha = 4^\circ, I = 0.28\%$.

in a higher L and lower D. Figure 6a shows the pressure coefficient C_p along the chord of the airfoil. LES and 2D URANS predicted the lowest and the highest pressure plateau, which is correlated with the LSB, and the maximum and minimum L, respectively. The reattachment is correlated with the point of maximum pressure gradient downstream of the plateau. Figure 6b shows large differences between the streamwise C_f values computed by the different models. The reattached thinner and more energetic boundary layer predicted by LES is correlated with a significantly increased C_f. However this does not result in a higher D because the friction drag is more than one order of magnitude smaller than the pressure drag.

In conclusion, a comparison of the experimental flow measurements and the LES, 3D URANS and 2D URANS solutions shows that while LES provides the most accurate solution, the bi-dimensionality of the 2D URANS simulations do not lead to a significant increase in the modelling error when compared with 3D URANS. Importantly, the 2D URANS simulations are capable of correctly predicting the general features of the LSB.

Optimum airfoil shapes

Since the above results have grown our confidence in the numerical results achieved with 2D URANS simulations, we now consider the optimum airfoil geometry computed for different Re. For each Re from 10^4 to 3×10^6, figure 7 shows the optimum geometry and the correlated velocity field $|\boldsymbol{u}|/U_\infty$. At the lowest value of Re investigated, $Re = 10^4$, the boundary layer is laminar and the optimum airfoil presents a very small curvature for most of the chord in order to delay separation, which occurs on the upper side at $x_s/c = 0.81$. Downstream of the separation point, the curvature increases in order to generate lift. At $Re = 3 \times 10^4$, laminar separation does not occur, therefore a higher curvature may be exploited in the first half of the chord for lift generation. The flatter trailing edge then prevents separation over the second half of the chord. At $Re = 10^5$, we find a

DOI: 10.1002/fld

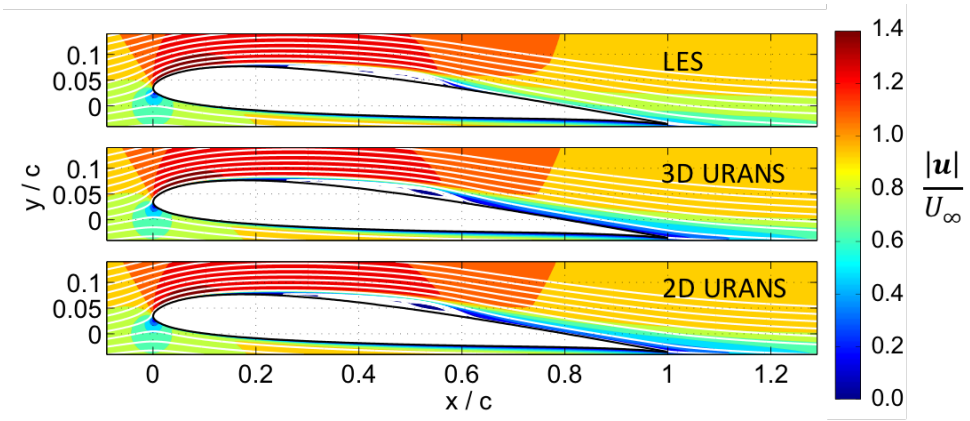

Figure 5. Contours of velocity and streamlines around the SD7003 airfoil at $Re = 6 \times 10^4, \alpha = 4^\circ, I = 0.28\%$.

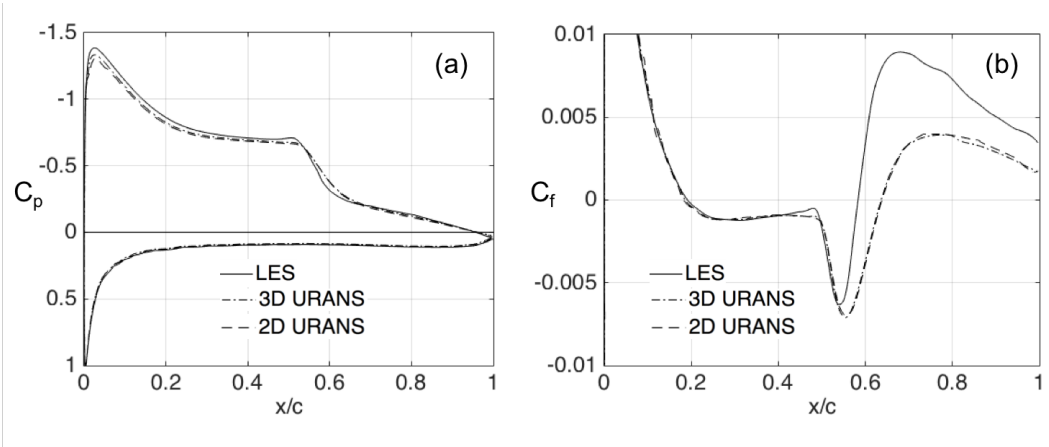

Figure 6. (a) Pressure coefficient and (b) streamwise friction coefficient for the SD7003 airfoil tested at $Re = 6 \times 10^4, \alpha = 4^\circ, I = 0.28\%$.

long LSB. Near the leading edge, a high curvature provides lift but in this case promotes separation ($x_s/c = 0.25$), while downstream of the separation point the airfoil has almost no curvature to promote turbulent reattachment ($x_r/c = 0.65$) and the formation of a long LSB. At $Re = 3 \times 10^5$, a more uniform curvature allows the separation point to be further downstream ($x_s/c = 0.61$); transition occurs closer to the separation point leading to a shorter LSB ($x_r/c = 0.75$) and an advantageous thinner wake. At $Re = 10^6$, transition occurs in the attached boundary layer; the turbulent boundary layer remains attached along the entire airfoil. An almost constant curvature on the upper side leads to a very thin wake and low drag. Finally, at the highest Re evaluated, $Re = 3 \times 10^6$, the increased resilience of the turbulent boundary layer to separation allows the area of highest curvature, and thus highest adverse pressure gradient, to be moved furthest toward the trailing edge. This again has the additional advantage of minimising wake thickness and thus drag.

Maximum efficiency

The wake's thickness, which is correlated with the drag, decreases monotonically with Re despite the complex relationship between the flow field, the airfoil geometry and the Reynolds number. Noting that $C_L = 0.6$ at every Re, the decrease in wake thickness results in an increase of L/D with Re. In figure 8, we compare the our results (black filled dots) achieved optimising the airfoil shape for every Re, with those of other authors that tested individual airfoils across a range of

DOI: 10.1002/fld

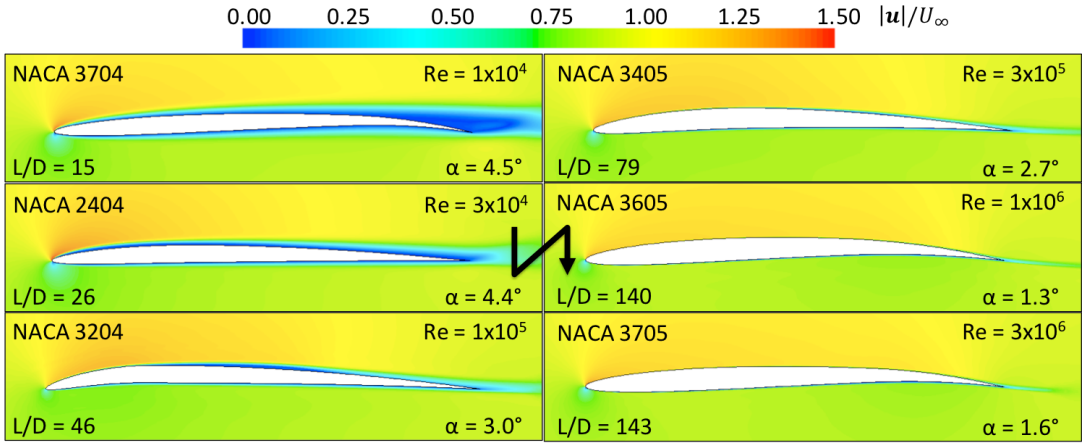

Figure 7. Contours of flow speed around the optimum airfoils for different Re.

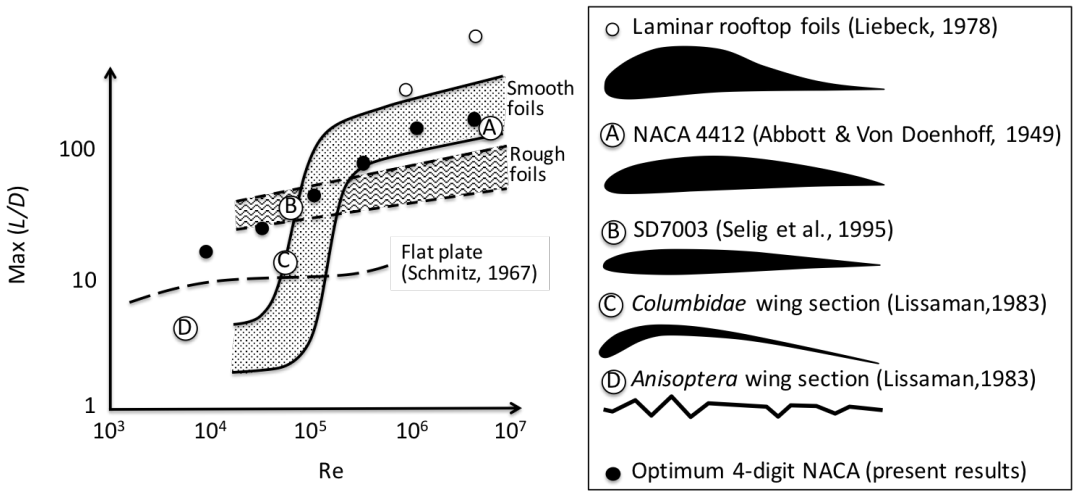

Figure 8. Airfoil efficiency for a range of Reynolds numbers from the literature and present results.

Re. For example, McMaster *et al.* (McMasters and Henderson 1980) identified an interval of Re between 10^4 and 10^6 (region between solid lines marked with dots), where the L/D of most smooth airfoils increases from less than 10 to more than 100. Conversely, rough foils have a more gentle increase of L/D versus Re (region between short dash lines marked with waves), due to their ability to promote transition near the leading edge. Similarly, Schmitz (Schmitz 1967) found that flat plates have a smoother L/D trend (long dash line) because leading edge separation promotes transition.

At the lowest Re tested, $Re = 10^4$, the 4-digit NACA airfoils perform better than flat plates. However, the visual extrapolation of our results toward lower Re suggests that, at $Re = 10^3$, a 4-digit NACA airfoil would have similar performance than a flat plate. Our optimal airfoils have higher L/D than those presented by McMaster *et al.* (McMasters and Henderson 1980) at $Re = 10^4$ and 3×10^4, and similar L/D at $Re = 10^5$ and 10^6. This is not surprising given that the foils that McMaster *et al.* tested were optimised for critical and supercritical Re. Only specialised airfoils that adopt a 'laminar rooftop', such as those developed by Liebeck (Liebeck 1978), allow much higher efficiency at high Re.

DOI: 10.1002/fld

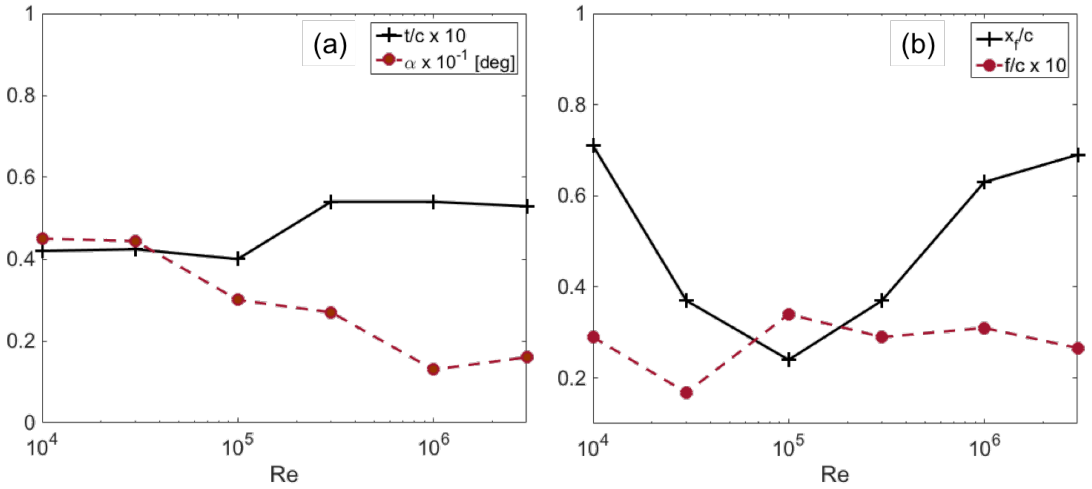

Figure 9. Trends of the design variables with Re.

Optimum thickness

It has been observed that thinner airfoils allow higher efficiency than thicker airfoils at low Re. Lilienthal (Lilienthal 1911), who studied bird wings at low Re, noted for the first time that curved thin plates performed better than thick airfoils. When the influence of Re was then better understood, it was found that airfoil efficiency increases with Re, and eventually exceeds that of thin plates (Schmitz 1967). Sunada *et al.* (S. Sunada, Sakaguchi, and Kawachi 1997; S Sunada et al. 2002) tested a range of airfoils and flat and curved plates at $Re = 4 \times 10^3$ and found that, at such low Re, the curved plates are the most efficient. Lissaman (Lissaman 1983) compared wing sections of efficient fliers at increasing Re: from insects, through birds, to aircraft, and noted that the thickness-to-chord ratio of these sections increased with Re. Figure 8 shows the efficiency of the dragonfly *Anisoptera*, the pigeon *Columbidae*, the SD7003 and the NACA4412, which all fit the trend suggested by McMasters *et al.* (McMasters and Henderson 1980) for smooth airfoils.

The proposed monotonic increase of t/c with Re is not confirmed by present results. In fact, as shown in figure 9a, t/c is roughly a step function of Re, with the step occurring between $Re = 10^5$ and 3×10^5; the point from which with increasing Re the boundary layer remains attached along the entire airfoil. The trend of x_f/c with Re is also non monotonic: x_f/c decreases when trailing edge separation occurs, and then increases for higher Re (figure 9b). Conversely, $f/c \approx 3\%$ for every Re. Therefore, we conclude that in order to generate a constant $C_L = 0.6$, the optimal camber remains constant while the angle of attack is varied to achieve the desired lift.

CONCLUSIONS

In this paper we propose a numerical model for the optimisation of airfoils across a range of Reynolds numbers (Re) from 10^4 to 3×10^6. We consider 2D unsteady incompressible flow, a $\gamma - Re_{\theta_t}$ transition model with a $\kappa - \omega$ SST turbulence model, and we couple the fluid solver with a covariance matrix adaptation evolutionary optimisation algorithm. We use this approach to find the optimal 4-digit NACA airfoil that maximises the lift-over-drag ratio allowing an arbitrary chosen lift coefficient of 0.6.

We investigate the numerical and modelling errors performing 3D simulations with the same numerical setup, Large Eddy Simulations and Xfoil simulations, in addition to comparisons with experimental data available in the literature. We show that the 2D simulations allow the prediction of the separation, transition and reattachment within approximately 10% of the chord compared with experimental data. In the range of validity of Xfoil, i.e. when natural laminar-to-turbulent

DOI: 10.1002/fld

transition occurs and separation is limited within a laminar separation bubble, it shows comparable performances. The 3D simulations do not offer a significant improvement compared to the 2D simulations, while the Large Eddy Simulations allows a better prediction of the transition and reattachment locations.

At transitional Reynolds numbers, the largest numerical uncertainty is the one due to the grid resolution and it decreases with Re. For the lift coefficient, it ranges from 8% to 0.003%, and for the drag coefficient it ranges from 19% to 2%. We find approximately the same grid uncertainties also for a similar test case of an SD7003 airfoil at $Re = 6 \times 10^4$, where experimental data is available. For this case, the uncertainties due to the time resolution, the round off error and the convergence are all more than one order of magnitude smaller. These level of uncertainty are sufficiently small to evaluate the performances of an airfoil across the range of Re considered. In fact, the lift-over-drag ratio of the optimal 4-digit NACA airfoils increases by 300% for every tenfold increase in Re.

It has been observed that the thickness-to-chord ratio of wing sections of efficient fliers, both man made and natural, increases monotonically with Re. Our results, however, show that the optimal thickness does not increase monotonically. On the contrary, it is almost constant at low and high Re, and shows a step increase when Re is sufficiently high to prevent separation or to allow reattachment and the formation of a laminar separation bubble. In order to generate a constant lift coefficient, which is largely dictated by angle of attack and camber, the angle of attack decreases monotonically with Re, while the camber remains ca. 3% at every Re. These results suggest that the airfoil shapes of insect and bird wings, that are the consequence of natural evolution, may not be aerodynamic optima when considering solely the maximisation of lift-to-drag ratio.

REFERENCES

Barbarino, S. et al. (2011). *A review of morphing aircraft*. DOI: 10.1177/1045389X11414084.

Barlas, T. K. and G.A.M. van Kuik (2010). *Review of state of the art in smart rotor control research for wind turbines*. DOI: 10.1016/j.paerosci.2009.08.002.

Biancolini, M.E. (2018). *Fast Radial Basis Functions for Engineering Applications*. Springer International Publishing. ISBN: 978-3-319-75009-5. DOI: 10.1007/978-3-319-75011-8.

Biancolini, M.E., E. Costa, et al. (2016). "Glider fuselage-wing junction optimization using CFD and RBF mesh morphing". In: *Aircraft Engineering and Aerospace Technology*. DOI: 10.1108/aeat-12-2014-0211.

Biancolini, M.E., I.M. Viola, and M. Riotte (2014). "Sails trim optimisation using CFD and RBF mesh morphing". In: *Computers & Fluids*. DOI: 10.1016/j.compfluid.2014.01.007.

Bot, P. et al. (2016). "Sharp Transition in the Lift Force of a Fluid Flowing Past Nonsymmetrical Obstacles: Evidence for a Lift Crisis in the Drag Crisis Regime". In: *Physical Review Letters* 117.23. ISSN: 10797114. DOI: 10.1103/PhysRevLett.117.234501.

Carmichael, B.H. and NASA (1982). "Low Reynolds number airfoil survey". In: *NASA Contractor Report* 1. DOI: doi:10.2514/1.25431.

Catalano P.and Tognaccini, R. (2010). "Numerical analysis of the flow around the SD 7003 airfoil". In: *48th AIAA Aerospace Sciences Meeting Including the New Horizons Forum and Aerospace Exposition*, p. 68.

Celik, I. (2003). "RANS/LES/DES/DNS: The Future Prospects of Turbulence Modeling". In: *Journal of Fluids Engineering* 127, pp. 829–830. ISSN: 0098-2202. DOI: 10.1115/1.2033011.

Chapin, V., N. De Carlan, and P. Heppel (2011). "Performance optimization of interacting sails through fluid structure coupling." In: *International Journal of Small Craft Technology* 153.Part B2, pp. 103–116. URL: http://oatao.univ-toulouse.fr/5262/.

Crabtree, L.F. (1959). *The formation of regions of separated flow on wing surfaces*. HM Stationery Office.

Drela, M. (1989). "XFOIL: An analysis and design system for low Reynolds number airfoils". In: *Low Reynolds number aerodynamics*. Springer, pp. 1–12.

– (1998). “Pros and Cons of Airfoil Optimization”. In: *Proceedings of Frontiers of Computational Fluid Dynamics*, pp. 1–19. DOI: 10.1142/9789812815774.

Hansen, M.O.L. et al. (2006). *State of the art in wind turbine aerodynamics and aeroelasticity*. DOI: 10.1016/j.paerosci.2006.10.002. arXiv: arXiv:1006.4405v1.

Hansen, Nikolaus et al. (2011). “Impacts of Invariance in Search: When CMA-ES and PSO Face Ill-conditioned and Non-separable Problems”. In: *Appl. Soft Comput.* 11.8, pp. 5755–5769. ISSN: 1568-4946. DOI: 10.1016/j.asoc.2011.03.001. URL: http://dx.doi.org/10.1016/j.asoc.2011.03.001.

Hicks, R.M. and P.A. Henne (1978). “Wing Design by Numerical Optimization”. In: *Journal of Aircraft* 15.7, pp. 407–412. ISSN: 0021-8669. DOI: 10.2514/3.58379. URL: http://arc.aiaa.org/doi/10.2514/3.58379.

Hu, H. and M. Tamai (2008). “Bioinspired Corrugated Airfoil at Low Reynolds Numbers”. In: *Journal of Aircraft* 45.6, pp. 2068–2077. ISSN: 0021-8669. DOI: 10.2514/1.37173. URL: http://arc.aiaa.org/doi/10.2514/1.37173.

Ingen, J.L. van (2008). “The eˆN method for transition prediction. Historical review of work at TU Delft”. In: *38th AIAA Fluid Dynamics Conference and Exhibit*. AIAA 2008-3830, pp. 1–49. ISBN: 9781563479427. DOI: AIAA2008-3830.

Klanfer, L. and P.R. Owen. *The effect of isolated roughness on boundary layer transition*.

Kuder, I.K. et al. (2013). *Variable stiffness material and structural concepts for morphing applications*. DOI: 10.1016/j.paerosci.2013.07.001.

Lachenal, X., S. Daynes, and P.M. Weaver (2013). *Review of morphing concepts and materials for wind turbine blade applications*. DOI: 10.1002/we.531. arXiv: arXiv:1006.4405v1.

Langtry, R. and F. Menter (2005). “Transition Modeling for General CFD Applications in Aeronautics”. In: *43rd AIAA Aerospace Sciences Meeting and Exhibit*. DOI: 10.2514/6.2005-522.

Liebeck, R.H. (1978). “Design of Subsonic Airfoils for High Lift”. In: *Journal of Aircraft* 15.9, pp. 547–561. ISSN: 0021-8669. DOI: 10.2514/3.58406. URL: http://arc.aiaa.org/doi/10.2514/3.58406.

Lilienthal, O. (1911). *Birdflight as the Basis of Aviation: A Contribution Towards a System of Aviation, Compiled from the Results of Numerous Experiments Made by O. and G. Lilienthal*. Longmans, Green.

Lissaman, P.B.S. (1983). “Low-Reynolds-Number Airfoils”. In: *Annual Review of Fluid Mechanics* 15.1, pp. 223–239. ISSN: 0066-4189. DOI: 10.1146/annurev.fl.15.010183.001255. URL: http://www.annualreviews.org/doi/10.1146/annurev.fl.15.010183.001255.

Mack, L.M. (1977). “Transition and Laminar Instability”. In: *Jet Propulsion Laboratory Pub.* Pp. 77–115.

McMasters, J. and M. Henderson (1980). “Low-speed single-element airfoil synthesis”. In: *Technical Soaring* 6.2, pp. 1–21.

Menter, F.R., R. Langtry, and S. Völker (2006). “Transition modelling for general purpose CFD codes”. In: *Flow, turbulence and combustion* 77.1-4, pp. 277–303.

Minervino, M., P.L. Vitagliano, and D. Quagliarella (2016). “Helicopter stabilizer optimization considering rotor downwash in forward-flight”. In: *Aircraft Engineering and Aerospace Technology* 88.6, pp. 846–865. ISSN: 0002-2667. DOI: 10.1108/AEAT-03-2015-0082. URL: http://www.emeraldinsight.com/doi/10.1108/AEAT-03-2015-0082.

Moin, P. and K. Mahesh (1998). “DIRECT NUMERICAL SIMULATION: A Tool in Turbulence Research”. In: *Annual Review of Fluid Mechanics* 30.1, pp. 539–578. ISSN: 0066-4189. DOI: 10.1146/annurev.fluid.30.1.539. URL: http://www.annualreviews.org/doi/10.1146/annurev.fluid.30.1.539.

O. Smith, A. M. (1975). “High-Lift Aerodynamics”. In: *Journal of Aircraft* 12.6, pp. 501–530. ISSN: 0021-8669. DOI: 10.2514/3.59830. URL: http://arc.aiaa.org/doi/10.2514/3.59830.

Ol, M. et al. (2005). "Comparison of laminar separation bubble measurements on a low Reynolds number airfoil in three facilities". In: *35th AIAA fluid dynamics conference and exhibit*, p. 5149.

Pasquale, D.Di, A. Rona, and S.J. Garrett (2009). "A selective review of CFD transition models". In: *39th AIAA Fluid Dynamics Conference* June, AIAA 2009–3812. DOI: 10.2514/6.2009-3812. URL: http://arc.aiaa.org/doi/pdf/10.2514/6.2009-3812.

Radespiel, R.E., J. Windte, and U- Scholz (2007). "Numerical and experimental flow analysis of moving airfoils with laminar separation bubbles". In: *AIAA journal* 45.6, pp. 1346–1356.

Roache, P.J. (1998). "Verification of codes and calculations". In: *AIAA Journal* 36, pp. 696–702. ISSN: 0001-1452. DOI: 10.2514/3.13882. URL: http://arc.aiaa.org/doi/abs/10.2514/3.13882.

Sagaut, P. and S. Deck (2009). "Large eddy simulation for aerodynamics: status and perspectives". In: *Philosophical Transactions of the Royal Society of London A: Mathematical, Physical and Engineering Sciences* 367.1899, pp. 2849–2860. ISSN: 1364-503X. DOI: 10.1098/rsta.2008.0269. eprint: http://rsta.royalsocietypublishing.org/content/367/1899/2849.full.pdf. URL: http://rsta.royalsocietypublishing.org/content/367/1899/2849.

Schmitz, F.W. (1967). "Aerodynamics of the model airplane. Part 1-Airfoil measurements". In:

Selig, M.S. (1995). *Summary of Low Speed Airfoil Data*. Summary of Low Speed Airfoil Data v. 1. SoarTech Publications. ISBN: 9780964674714. URL: https://books.google.it/books?id=qtIeAQAAIAAJ.

– (2003). "Low Reynolds Number Airfoil Design Lecture Notes - Various Approaches to Airfoil Design". In: *VKI Lecture Series* November, pp. 24–28. URL: http://www.ae.illinois.edu/m-selig/pubs/Selig-2003-VKI-LRN-Airfoil-Design-Lecture-Series.pdf.

Smirnov, A., S. Shi, and I. Celik (2001). "Random Flow Generation Technique for Large Eddy Simulations and Particle-Dynamics Modeling". In: *Journal of Fluids Engineering* 123.2, p. 359. ISSN: 00982202. DOI: 10.1115/1.1369598. URL: http://fluidsengineering.asmedigitalcollection.asme.org/article.aspx?articleid=1429342.

Smith, A.M.O. (1956). *Transition, Pressure Gradient, and Stability Theory*. DOI: ES26388.

Spalart, P.R. (2009). "Detached-Eddy Simulation". In: *Annual Review of Fluid Mechanics* 41.1, pp. 181–202. ISSN: 0066-4189. DOI: 10.1146/annurev.fluid.010908.165130. URL: http://www.annualreviews.org/doi/10.1146/annurev.fluid.010908.165130.

Squires, K.D. (2004). "Detached-eddy simulation: Current status and perspectives". In: *Direct and Large-Eddy Simulation V, Proceedings* 9, pp. 465–480. DOI: 10.1146/annurev.fluid.010908.165130.

Srinath, D.N. and S. Mittal (2010). "Optimal aerodynamic design of airfoils in unsteady viscous flows". In: *Computer Methods in Applied Mechanics and Engineering* 199.29-32, pp. 1976–1991. ISSN: 00457825. DOI: 10.1016/j.cma.2010.02.016.

Stanewsky, E. (2001). "Adaptive wing and flow control technology". In: *Progress in Aerospace Sciences* 37.7, pp. 583–667. ISSN: 03760421. DOI: 10.1016/S0376-0421(01)00017-3.

Sunada, S., A. Sakaguchi, and K. Kawachi (1997). "Airfoil section characteristics at a low Reynolds number". In: *Journal of fluids engineering* 119.1, pp. 129–135.

Sunada, S et al. (2002). "Comparison of wing characteristics at an ultralow Reynolds number". In: *Journal of aircraft* 39.2, pp. 331–338.

Tully, S. and I.M. Viola (2016). "Reducing the wave induced loading of tidal turbine blades through the use of a flexible blade". In: *International Symposium on Transport Phenomena and Dynamics of Rotating Machinery (ISROMAC 2016)*, p. 9.

Viola, I.M., P. Bot, and M. Riotte (2013). "On the uncertainty of CFD in sail aerodynamics". In: *International Journal for Numerical Methods in Fluids* 72.11, pp. 1146–1164. ISSN: 02712091. DOI: 10.1002/fld.3780. arXiv: fld.1 [DOI: 10.1002].

Ward, J.W. (1963). "The Behaviour and Effects of Laminar Separation Bubbles on Aerofoils in Incompressible Flow". In: *Journal of the Royal Aeronautical Society* 67, pp. 783–790. ISSN: 0368-3931. DOI: https://doi.org/10.1017/S0001924000061583.

Wu, X. and P. Moin (2009). "Direct numerical simulation of turbulence in a nominally zero-pressure-gradient flat-plate boundary layer". In: *Journal of Fluid Mechanics* 630, pp. 5–41. ISSN: 00221120. DOI: 10.1017/S0022112009006624.

Zhang, W., R. Hain, and C.J. Kähler (2008). "Scanning PIV investigation of the laminar separation bubble on a SD7003 airfoil". In: *Experiments in Fluids* 45.4, pp. 725–743. ISSN: 07234864. DOI: 10.1007/s00348-008-0563-8.